



## Article

# Mapping Phenology of Complicated Wetland Landscapes through Harmonizing Landsat and Sentinel-2 Imagery

Chang Fan <sup>1</sup>, Jilin Yang <sup>2</sup>, Guosong Zhao <sup>3</sup>, Junhu Dai <sup>2</sup>, Mengyao Zhu <sup>2</sup>, Jinwei Dong <sup>2</sup>, Ruoqi Liu <sup>1</sup> and Geli Zhang <sup>1,\*</sup>

<sup>1</sup> College of Land Science and Technology, China Agricultural University, Beijing 100193, China; chang.fan@cau.edu.cn (C.F.); ruoqi.liu@cau.edu.cn (R.L.)

<sup>2</sup> Institute of Geographic Science and Natural Resources Research, Chinese Academy of Sciences, Beijing 100101, China; yangjl.17b@igsrr.ac.cn (J.Y.); daijh@igsrr.ac.cn (J.D.); zhummy.18b@igsrr.ac.cn (M.Z.); dongjw@igsrr.ac.cn (J.D.)

<sup>3</sup> School of Geography and Information Engineering, China University of Geosciences, Wuhan 430074, China; zhaoguosong@cug.edu.cn

\* Correspondence: geli.zhang@cau.edu.cn; Tel.: +86-188-1317-6102

**Abstract:** Wetlands are important CO<sub>2</sub> sinks and methane sources, and their seasonality and phenological cycle play an essential role in understanding the carbon budget. However, given the spatial heterogeneity of wetland landscapes and the coarser spatial resolution of satellites, the phenological retrievals of wetlands are challenging. Here we examined the phenology of wetlands from 30 m harmonized Landsat/Sentinel-2 (LandSent30) and 500 m MODIS satellite observations using the ground phenology network PhenoCam as a benchmark. This study used all 11 available wetland PhenoCam sites (about 30 site years), covering diverse wetland types from different climate zones. We found that the LandSent30-based phenology results were in overall higher consistency with the PhenoCam results compared to MODIS, which could be related to the better explanation capacity of LandSent30 data in the heterogeneous landscapes of wetlands. This also means that the LandSent30 has an advantage over the 500 m MODIS regarding wetland vegetation phenological retrievals. It should be noted that the LandSent30 did not show a greatly improved performance, which could be related to the specificity and complexity of the wetlands landscape. We also illustrated the potential effects of the location and observation direction of PhenoCam cameras, the selection of Region of Interest (ROI), as well as the landscape composition of the site. Overall, this study highlights the complexity of wetland phenology from both ground and remote sensing observations at different scales, which paves the road for understanding the role of wetlands in global climate change and provides a basis for understanding the real phenological changes of wetland surfaces.

**Keywords:** wetlands; phenology; PhenoCam; Landsat; Sentinel-2; MODIS



**Citation:** Fan, C.; Yang, J.; Zhao, G.; Dai, J.; Zhu, M.; Dong, J.; Liu, R.; Zhang, G. Mapping Phenology of Complicated Wetland Landscapes through Harmonizing Landsat and Sentinel-2 Imagery. *Remote Sens.* **2023**, *15*, 2413. <https://doi.org/10.3390/rs15092413>

Academic Editor: Frédéric Frappart

Received: 22 March 2023

Revised: 27 April 2023

Accepted: 28 April 2023

Published: 5 May 2023



**Copyright:** © 2023 by the authors. Licensee MDPI, Basel, Switzerland. This article is an open access article distributed under the terms and conditions of the Creative Commons Attribution (CC BY) license (<https://creativecommons.org/licenses/by/4.0/>).

## 1. Introduction

Vegetation phenology is a crucial driver of the seasonality of ecosystem processes and an important indicator of the terrestrial response to climate change [1,2]. Wetlands are one of the most important ecosystems and play an essential role in maintaining biodiversity [3–7]. Wetlands also influence global and local climate through their role as carbon sinks, which absorb CO<sub>2</sub> and carbon sources that emit CH<sub>4</sub> [8,9]. For example, the growing season of alpine wetland vegetation in the Tibetan Plateau has been extended with the increasing temperature [10], and this phenological shifting has further enhanced the growth and productivity of wetland vegetation and positively influenced the carbon sink of alpine wetland ecosystems [11]. Studies in the tropics have also shown that the phenological cycle plays a crucial role in CH<sub>4</sub> emissions from wetlands [12,13]. Therefore, wetland phenology information is essential for understanding the role of wetland ecosystems in global climate change and carbon cycling processes.

However, wetland vegetation often grows in unique environments with alternating terrestrial and aquatic ecosystems and a high diversity of biological types [14,15], which makes local wetland phenological observations difficult. Traditionally, two main methods are used to obtain surface vegetation phenology; one is in situ phenological observation, such as manual observation records and near-surface digital repeat photography-based observations (e.g., PhenoCam, smartphone) [16–18]. Another is vegetation phenology estimation based on satellite remote sensing data [19]. Although manual phenology observation records have a higher accuracy, they usually have a small observation range, subjective tendency, and high cost, which makes it difficult to achieve practical observation over a wide range of long time series [20,21]. In contrast, remote sensing data provide measurements ranging from site-based observations to global-scale measurements from satellite-based missions [22–24].

In the past few decades, continuous advances in satellite remote sensing technology have provided great opportunities for land use and land cover change monitoring as well as phenology analysis studies of different land types. Moderate Resolution Imaging Spectroradiometer (MODIS) inversion-based phenology methods are widely used for phenology analysis and monitoring on large and long timescales. For example, MODIS data have been broadly used for capturing the phenology of deciduous forests [25,26], grasslands [27,28], rice paddies [29], and mangroves [30], which helps to monitor and understand vegetation dynamics. MODIS-based phenological products such as MCD12Q2, the global vegetation phenological product, have also been generated and evaluated based on ground-based measurements [31]. These different surface phenological studies and products have contributed to further analysis of the biological effects of global climate change and land use monitoring. However, the coarse spatial resolution of MODIS is susceptible to the influence of mixed pixels. It does not reflect the surface vegetation signal well, which may limit the retrieval of vegetation phenology in areas with high landscape heterogeneity [31,32]. In addition, coastal wetlands often suffer from frequent flooding caused by the tidal environment, which means the spectrum of wetland vegetation has high variability over a short time, thus weakening the signal of wetland vegetation [33–35]. Therefore, large uncertainties still exist in retrieving wetland phenology based on satellite remote sensing [5].

The successful launch of the Landsat and Sentinel satellites with high spatial and temporal resolutions has provided new opportunities for more accurate phenological retrievals [36], attracting widespread attention [37]. For example, Landsat data have been used for tracking the phenology of deciduous forests [36], grasslands [38], rice [39], wetlands [40], and croplands [41,42] at local scales, which has added new vigor to vegetation phenology studies with finer spatial details. Landsat-based data have also generated regional phenology products such as 30 m annual vegetation phenology datasets in Northern America [37,43,44]. Therefore, the seasonal patterns of different vegetation phenology metrics were portrayed. Melaas [44] used all available Landsat valid images to retrieve vegetation phenology metrics and demonstrated that Landsat provided finer spatial details of phenology information than MODIS.

Nevertheless, to our knowledge, the phenological retrievals of wetland vegetation (PWV) at 30 m resolution have not been well investigated. Therefore, it is urgent to use finer satellite data to estimate PWV better to understand the interaction between climate change and wetland vegetation [45]. However, even though satellite remote sensing continues to break through in terms of temporal and spatial resolution, satellite-based methods are inevitably interfered with by signals from atmospheric conditions such as clouds and snow [31,46]. There are uncertainties in the agreement between the actual conditions occurring on the surface and those observed by satellite sensors [20]. Therefore, whether the near-surface vegetation phenology interpreted by various sensors is consistent with ground observations has also received unanimous attention from the community [38,47–49]. The PhenoCam network was established in 2008 and now has over 700 sites, initially providing automated near-surface canopy remote sensing for the northeastern United States and neighboring

Canada, and has since evolved to provide near-surface phenology monitoring on a global scale [50]. In recent decades, the PhenoCam network of sites has offered technical support for near-surface vegetation phenology research worldwide and free site observations in remote areas that are difficult to reach or access, pushing vegetation phenology research to new heights [51]. Therefore, the release of the PhenoCam network provided a sufficient data source for this study and was seen as a bridge between traditional methods of in situ manual observation of vegetation phenology and remote sensing-based phenology estimation Klosterman, et al. [52].

Here, we provided a method for estimating PWV and compared the differences between two sets of satellite data (LandSent30 and 500 m MODIS) with different spatial resolutions using PhenoCam data. Specifically, we first selected and filtered global wetland PhenoCam sites and calibrated their locations through site-by-site metadata and photo checks. Second, we fused multi-source satellite data (LandSent30) to accurately extract the time series of three widely used vegetation indices (NDVI, EVI, and NIRv) for each wetland PhenoCam site. Further, we estimated the vegetation phenological metrics of each site using a double logistic function (DLF) model. Eventually, we explored the differences between satellite sensor-based PWV and near-surface observation-based PWV. This study aims to answer two questions: (1) Can wetland vegetation phenology estimated by LandSent30 remote sensing data accurately capture near-surface vegetation phenology? (2) What are the differences in the performance of the satellite sensing data with different resolutions in retrieving PWV? Our study provides a reference for global observational studies of wetland phenology and a basis for understanding the role of wetlands in climate change.

## 2. Materials and Methods

### 2.1. Study Area

Wetland vegetation is widely distributed worldwide and includes marshes, swamps, mangroves, tidal flats, and other types. In this study, we selected 11 sites from the global PhenoCam network based on the availability of near-surface digital camera observation wetland sites (Figure 1, Table 1). The sites are typical of wetland vegetation cover, where torrepalacio, donanafuenteduque, mayberry, juncabalejo, westpond, eastend, lostcreek, montebondonepeat, and merbleue sites cover marshes, and gcesapelo and northinletsalt-marsh sites cover salt marshes. The above sites are all located between 30°N and 50°N, mainly in the United States, Spain, and Italy, and are mainly located near the sea. These wetland sites involve various climate types, including seven sites with a Mediterranean climate, with hot and dry summers and mild and rainy winters; two sites with a humid subtropical climate, with hot and rainy summers and warm and wet winters; and two sites with a temperate continental climate, with hot and humid summers and cold and dry winters.

**Table 1.** Site characteristics of the PhenoCam sites used in this study.

Site	Latitude (°)	Longitude (°)	Altitude (m)	Start Date	End Date	Level <sup>1</sup>
donanafuenteduque	36.99855	−6.43460	1	1 January 2018	31 December 2018	I
eastend	38.10273	−121.64132	−5	1 January 2015	31 December 2017	I
gcesapelo	31.44404	−81.28353	0	1 January 2015	31 December 2018	I
juncabalejo	36.93619	−6.37845	1	1 January 2018	31 December 2018	I
lostcreek	46.08270	−89.97920	480	1 January 2017	31 December 2017	I
mayberry	38.04977	−121.76507	−5	1 January 2018	31 December 2018	II
merbleue	45.40940	−75.51870	69	1 January 2013	31 December 2018	I
montebondonepeat	46.01770	11.04090	1563	1 January 2015	1 January 2018	I
northinletsaltmarsh	33.34550	−79.19570	1	1 January 2018	31 December 2018	I
torrepalacio	36.99050	−6.44260	3	1 January 2018	31 December 2018	I
westpond	38.10742	−121.64687	−5	1 January 2013	31 December 2018	II

<sup>1</sup> Level I site follows the PhenoCam network standard protocol, and the PhenoCam is directly in contact with the researchers at the site (typically the highest quality data). Level II cameras do not follow the standard protocol, but the PhenoCam is still in contact with researchers at the site. Please see the PhenoCam website (<https://phenocam.nau.edu/webcam/> (accessed on 1 March 2022)) for more information.

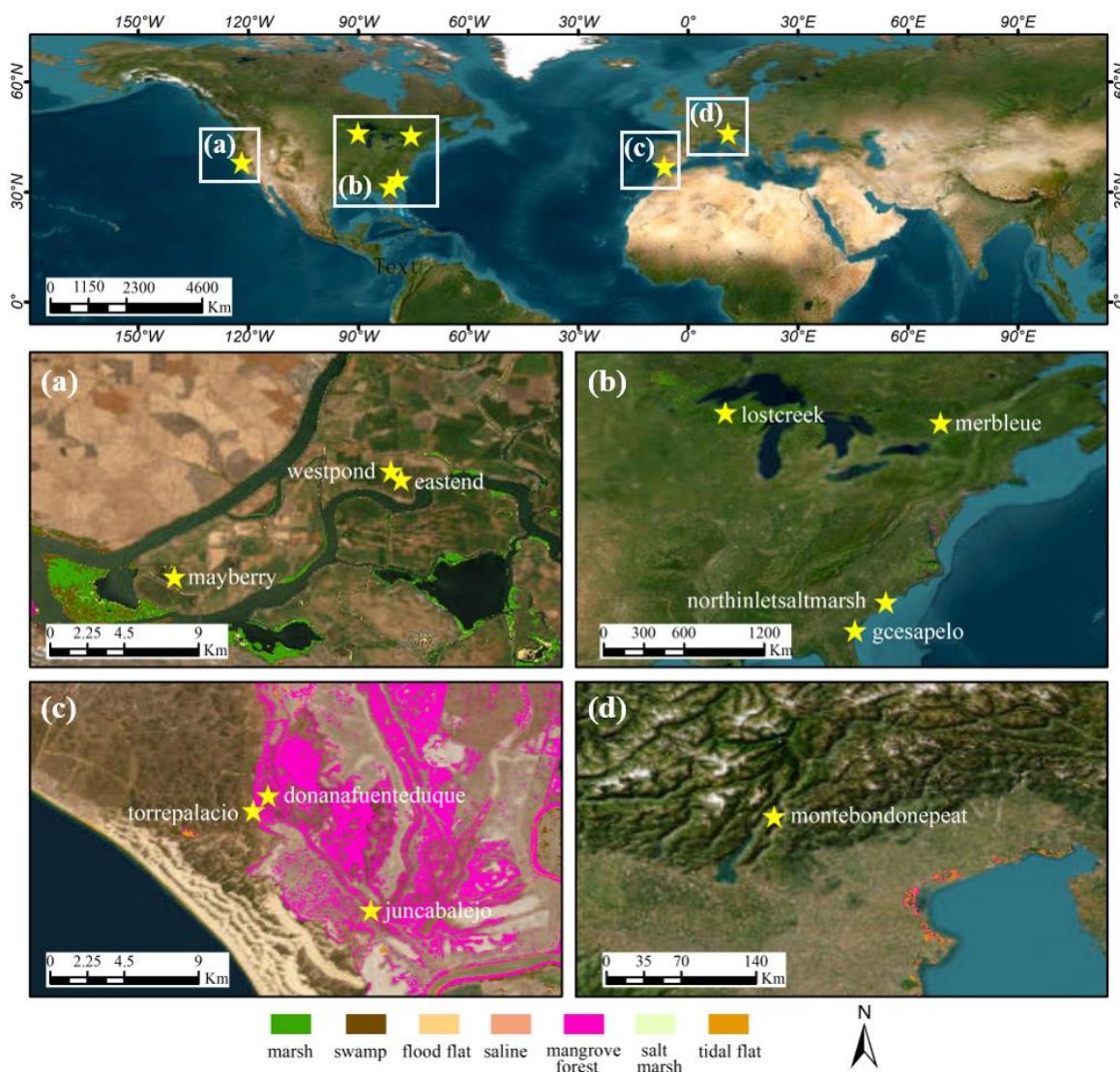


**Figure 1.** Wetland PhenoCam sites used in this study and their types. Figure (a–d) indicates the type of wetland vegetation at each site, respectively. The wetland sites are from the PhenoCam network, and the wetland types are from the global 30m wetland data (GWL\_FCS30) with a good classification system (<https://zenodo.org/record/6575731#.Y9afbnBBxEZ> (accessed on 10 January 2023)).

## 2.2. Data

### 2.2.1. Near-Surface Remote Sensing Data—PhenoCam Dataset

In this study, we used the PhenoCam Dataset v2.0 ([https://daac.ornl.gov/VEGETATION/guides/PhenoCam\\_V2.html](https://daac.ornl.gov/VEGETATION/guides/PhenoCam_V2.html) (accessed on 1 March 2022)) to validate the PWV of satellite remote sensing, which retrieves phenological metrics (the beginning of the growth period, later abbreviated as SOS, and the end of the growth period, later abbreviated as EOS) by analyzing time series of images of vegetation throughout the season [53]. Specifically, the phenology data analyzed were primarily from conventional visible wavelength images taken by high-resolution digital cameras installed at sites in the PhenoCam network. In addition, the network turns off the camera’s automatic white/color balance to minimize daily variations in scene illumination and exposure adjustment [50,53,54]. Most of the cameras take photos every 30 min and upload them to the PhenoCam server between 4:00 a.m. and 10:00 p.m. daily. The PhenoCam network extracts each image’s RGB color channel information using simple analysis techniques. It calculates pixel averages and other statistics over the region of interest (ROI) to form time series characterizing vegetation color at 1-day and 3-day intervals, such as robustness index green chromatic

coordinate (GCC) [52,55]. Then, a spline function interpolation method was used to retrieve the greenness rise and fall phenological metrics corresponding to the GCC time series at different amplitudes. The dataset is widely used in the validation of phenology models and the evaluation of satellite data products [18,48,56].

$$GCC = \frac{G_{DN}}{R_{DN} + G_{DN} + B_{DN}} \quad (1)$$

where GCC is the green chromatic coordinate often used in phenology analysis, and  $R_{DN}$ ,  $G_{DN}$ , and  $B_{DN}$  are, respectively, the red, green, and blue color channels of the PhenoCam digital camera and represent digital numbers (DN) stored in JPEG format.

### 2.2.2. Landsat-7/8 and Sentinel-2A/B Data

Landsat-7 and 8 were successfully launched in 1999 and 2013, respectively, as extensions and continuations of the previous generation of Landsat satellites [57], carrying the Enhanced Thematic Mapper Plus (ETM+), the Operational Land Imager (OLI), and the Thermal Infrared Sensor (TIS). They rotate around the Earth in a Sun-synchronous near-polar orbit and repeat observations every 16 days, providing a wide range of continuous land surface observations at a spatial resolution of 30 m [58], which can further contribute to understanding the Earth's system and its response to natural and anthropogenic changes and improve our ability to predict climate and natural disasters [59]. Sentinel-2A/B was successfully launched in 2015 and 2017, respectively, offering improved spatial, temporal, and spectral resolution [60]. It is a wide-field, high-resolution, multispectral imaging mission widely used to monitor vegetation, soil, and water cover and observe environmental conditions and changes in inland waterways and coastal areas [61].

We selected three commonly used vegetation indices (normalized difference vegetation index (NDVI), enhanced vegetation index (EVI), and near-infrared reflectance of vegetation (NIRv), respectively) to compare with the seasonal dynamic trajectories of the PhenoCam-GCC index. The three vegetation indices were calculated as follows:

$$NDVI = \frac{\rho_{NIR} - \rho_{RED}}{\rho_{NIR} + \rho_{RED}} \quad (2)$$

$$EVI = 2.5 \times \left( \frac{\rho_{NIR} - \rho_{RED}}{\rho_{NIR} + 6 \times \rho_{RED} - 7.5 \times \rho_{BLUE} + 1} \right) \quad (3)$$

$$NIRv = NDVI \times \rho_{NIR} \quad (4)$$

where  $\rho_{BLUE}$ ,  $\rho_{RED}$ , and  $\rho_{NIR}$  are the reflectance values from the blue (450–515 nm), red (630–680 nm), and NIR (845–885 nm) bands, respectively.

### 2.2.3. MODIS Data

MODIS data were used in this study to investigate the differences in the retrieval of the PWV from different satellite remote sensing resolution data. We first calculated the MODIS-based vegetation indices from wetland sites provided by the PhenoCam network. Then, we compared the seasonal dynamics between MODIS-based vegetation indices and PhenoCam-GCC-based indices. The MCD43A4 Version 6 Nadir Bidirectional Reflectance Distribution Function (BRDF)-Adjusted Reflectance (NBAR) dataset is a daily product at a 500 m spatial resolution. It combines Terra and Aqua spacecraft, selecting the best representative pixels from 16 days, widely used to characterize vegetation dynamics. Additionally, the NBAR measurements are based on surface reflectance from a 16-day moving window of MODIS data, are correlated with the middle day of the 16-day synthetic period, and are generated every eight days [62].

The NBAR data were filtered to remove observations of urban areas, clouds, ice, or water using the MODIS MCD12Q1 land cover type product. Additionally, the remaining data were filtered to remove snow disturbances using the MODIS BRDF albedo quality

product (MCD43A2). The filtered MCD43A4 dataset was used to calculate three typical vegetation indices (NDVI, EVI, NIRv) at each wetland site, and the three vegetation indices were calculated using the following equations:

$$NBAR - NDVI = \frac{\rho_{NIR} - \rho_{RED}}{\rho_{NIR} + \rho_{RED}} \quad (5)$$

$$NBAR - EVI = 2.5 * \left( \frac{\rho_{NIR} - \rho_{RED}}{\rho_{NIR} + 6 * \rho_{RED} - 7.5 * \rho_{BLUE} + 1} \right) \quad (6)$$

$$NIRv - EVI = NDVI * \rho_{NIR} \quad (7)$$

where  $\rho_{RED}$ ,  $\rho_{BLUE}$ , and  $\rho_{NIR}$  correspond to MODIS Band 1 (620–670 nm), Band 3 (459–479 nm), and Band 2 (841–871 nm) spectral reflectance values, respectively.

### 2.3. Methods

#### 2.3.1. Screening and Correction of PhenoCam Sites

Considering the unique complexity of wetland landscapes, this paper filtered and calibrated the official wetland sites according to the rules of PhenoCam site specification and the rationality of selected ROI.

First, the sites were screened to remove wetland sites with severe offsets and non-conforming specifications. For example, the NEON.D07.WALK.DP1.20002 site has considerable landscape heterogeneity in the camera field of view, and the selected ROIs are mainly below the vegetation canopy. Therefore, the site was susceptible to substantial interference from surrounding forest signals in remote sensing-based PWV retrieval, so similar wetland sites were removed. Secondly, we calibrated all wetland sites on the Google Earth Engine platform (GEE) based on the official camera observation orientations. For example, the juncabalejo site recorded the northeast plot, limited by the fixed orientation of the camera (Figure 2). However, the satellite-based vegetation index time series characterize the two adjacent plots because of the cross-regional buffer generated by the center of the site. Therefore, in combination with the site ROI and camera observation orientations, we move the site's position to the northeast, the location shot by the PhenoCam network. The filed photos and details of the calibration wetland sites are shown in Figure 2 and Table 2.

Finally, we selected 11 wetland sites that met the requirements of this paper for approximately 30 site years, with a time range of 2013–2018. To compare with the LandSent30-based phenological metrics, we used the phenological periods at the 90% quantile of 3-day average composite GCC values corresponding to 10%, 25%, and 50% amplitudes to minimize the daily variation caused by weather conditions [55].

**Table 2.** Wetland sites and correction directions. lat\_correction and lon\_correction represent the corrected latitude and longitude, respectively.

Wetland Sites	Correction Direction	lat_Correction <sup>1</sup>	lon_Correction <sup>1</sup>
donanafuenteduque	-	36.99855	-6.43460
eastend	west	38.10276	-121.64203
gcesapelo	-	31.44404	-81.28353
juncabalejo	east	36.93624	-6.37631
lostcreek	-	46.08270	-89.97920
mayberry	west	38.04984	-121.76531
merbleue	-	45.40940	-75.51870
montebondonepeat	-	46.01770	11.04090
northinletsaltmarsh	-	33.34550	-79.19570
torrepalacio	north	36.99132	-6.44178
westpond	west	38.10734	-121.64739

<sup>1</sup> lat\_correction and lon\_correction represent the corrected latitude and longitude, respectively.



**Figure 2.** Example map of a PhenoCam wetland site to be calibrated and its camera field of view ROI. The blue circles indicate the 100 m radius around the area and the yellow boxes indicate the camera field of view ROI.

### 2.3.2. Landsat-7/8 and Sentinel-2 Data Fusion

Landsat-7/8 and Sentinel-2 SR data were atmospherically corrected in GEE, and we used the quality assessment (QA) (pixel\_qa) generated by CFMASK to remove the invalid observations of Landsat SR data, including cloud shadows, clouds, snow, etc. Meanwhile, we used a quality layer (QA60) for cloud mask preprocessing to identify and remove all bad-quality observations of Sentinel-2 data. Additionally, we also used the equation ( $LSWI > NDVI$ ) to eliminate flooding as well as snow-contaminated observations [63].

After quality control of the data, we fused Sentinel-2 and Landsat-7/8 satellite images from 2013–2018 based on the GEE platform. First, due to the slight difference in wavelength between the Landsat-7/8 and Sentinel-2 data, we chose to use Landsat-8 OLI data as the standard to fuse Landsat-7 ETM+ and Sentinel-2 MSI data (Table 3). In the ETM+ data, bands 1 (Blue), 3 (Red), 4 (NIR), and 5 (SWIR) were transformed using the ordinary least squares regression coefficient. In the MSI data, the NIR wavelength of band-8A matches better with band-8A of OLI, so the bands 2 (Blue), 4 (Red), 8A (NIR), and 11 (SWIR) in the Sentinel-2 MSI data were transformed using ordinary least squares regression coefficient [64]. To unify the spatial resolution of the three sensors, we used a bilinear interpolation method to resample ETM+ and MSI data to OLI data resolution (30 m spatial resolution). In addition, due to the repeated observations and side-by-side overlap between the images of each sensor, we generated a 10-day synthetic dataset of the maximum values of three vegetation indices (EVI, NDVI, and NIRv).

**Table 3.** The coefficients for data fusion in this study.

Bands	Landsat-7	Bands	Sentinel-2
Blue	$Land8^1 = 0.0003 + 0.8474 \times Land7^1$	Blue	$Land8^1 = 0.0003 + 0.9570 \times Sent2^1$
Red	$Land8^1 = 0.0061 + 0.9047 \times Land7^1$	Red	$Land8^1 = 0.0041 + 0.9533 \times Sent2^1$
NIR	$Land8^1 = 0.0412 + 0.8462 \times Land7^1$	NIR (Band8A)	$Land8^1 = 0.0077 + 0.9644 \times Sent2^1$
SWIR	$Land8^1 = 0.0254 + 0.8937 \times Land7^1$	SWIR	$Land8^1 = 0.0034 + 0.9522 \times Sent2^1$

<sup>1</sup> Landsat-8, Landsat-7 and Sentinel-2 are abbreviated as land8, land7, and Sent2 in the table, respectively. The fusion coefficients of each band are referenced from Zhang et al. [64].

### 2.3.3. Wetland Vegetation Phenological Metrics Estimation

The wetland vegetation phenological metrics (SOS, EOS) at different sites were estimated by the DLF method, which mainly includes interpolation filtering and smoothing operations on the original data [65]. Specifically, we first used the cubic spline interpolation and the modified Savitzky–Golay filter to process the missing and outlier values of each vegetation index’s original time series data [66]. Then, we used the DLF fitting method to smooth the above interpolated NDVI/EVI/NIRv data to generate daily NDVI/EVI/NIRv curves over the available years for each wetland site.

Finally, we estimated the SOS and EOS of wetland vegetation from the above reconstructed daily NDVI/EVI/NIRv curves for each wetland site. Furthermore, we analyzed the performance of the reconstructed vegetation index curves at different thresholds of amplitude (10%, 25%, and 50%). In this study, the SOS is defined as the first day on which the reconstructed day-by-day curves cross the predetermined amplitudes (10%, 25%, 50%), and EOS is defined as the last day of the corresponding year.

We chose Root Mean Square Error (RMSE), bias, and R-Square( $R^2$ ) statistics for all available data from wetland sites, which quantified the magnitude of differences and the degree of correlation between phenological periods from different sources.

$$R^2 = 1 - \frac{\sum_i (\hat{y}_i - y_i)^2}{\sum_i (\bar{y}_i - y_i)^2} \quad (8)$$

$$RMSE = \sqrt{\frac{1}{m} \sum_{i=1}^m (y_i - \hat{y}_i)^2} \quad (9)$$

$$Bias = \frac{1}{m} \sum_{i=1}^m (\hat{y}_i - y_i) \quad (10)$$

where  $m$  represents the number of stations,  $i$  represents the  $i$ th station,  $y_i$  represents the near-surface phenological observations, and  $\hat{y}_i$  represents the phenological period generated by satellite observations.  $R^2$  takes values in the range of [0, 1], and the closer the result is to 1, the better the model fits;  $RMSE$  takes values in the range of [0,  $+\infty$ ] and is equal to 0 when the fitted satellite-based phenological values match the near-surface perfectly, and the larger the error, the larger the value is. A high  $Bias$  means a poor match between the two, and a positive error represents a late period for satellite-based remote sensing.

### 2.3.4. Comparisons between Satellite- and PhenoCam-Based Phenology

In order to investigate PWV in complex terrain, we established different statistical range buffers (15 m, 30 m, 45 m, 60 m, 90 m, 120 m, and 150 m) within the GEE platform to extract remote sensing data time series from each wetland site. These buffers will be referred to as “extracted buffers” hereafter. For example, a 15 m extraction buffer refers to the process of extracting the vegetation index within a square area with sides measuring 30 m. After that, we extracted the phenological period of three wetland vegetation indices (EVI, NDVI, and NIRv) using different remote sensing data sources (LandSent30 and MODIS) at different extracted buffers. In addition, this study also focuses on comparing PWV for various remote sensing index thresholds (10%, 25%, 50%).

## 3. Results

### 3.1. Comparisons of before and after Consistency of Site Correction Positions

We calibrated the locations of five wetland sites: eastend, gcesapelo, mayberry, juncabalejo, and torrepalacio (Figure 3), and finally obtained around 30 wetland site years that met the data quality requirements. Here, the LanSent30-based PWV within a 15 m extracted buffer illustrates this study’s advantages in correcting the wetland site’s location (Table 4).



**Figure 3.** Correction of the location of the torrepalacio wetland site as an example. The left-hand image shows the location of the official PhenoCam network torrepalacio wetland site. The right-hand image shows the site correction, where the green dot indicates the original position, the blue dot indicates the corrected position, and the arrow indicates the direction of movement.

**Table 4.** Comparison of wetland phenology accuracy before and after correction of site location.

Remote Sensing Index	Statistic	SOS		EOS	
		Before	After	Before	After
NDVI	$R^2$	0.47	0.64	0.15	0.18
	RMSE	37.28	25.27	53.47	53.48
EVI	$R^2$	0.34	0.45	0.29	0.23
	RMSE	33.53	23.63	36.94	39.25
NIR <sub>v</sub>	$R^2$	0.37	0.49	0.26	0.24
	RMSE	29.84	22.9	37.09	37.94

Generally, we found that the accuracy of remote sensing-based PWV with correction of the site location was significantly improved on that without correction of the site location. The corrected Landsat30 metrics showed a strong linear relationship with the GCC phenological period provided by the PhenoCam network (Table 4), especially for the NDVI index. First, in the fitting results of the PWV, the corrected NDVI-SOS ( $R^2 = 0.64$ ,  $RMSE = 25.27$ ) was significantly better than that before correction ( $R^2 = 0.47$ ,  $RMSE = 37.28$ ), but the PWV-EOS improvement was not significant. Regarding the different GCC thresholds, the location-corrected SOS- $R^2$  for each threshold phenological period was generally higher than before the correction. The RMSE was also smaller than before the correction, especially for the 10% GCC threshold (Figures S1–S3). Focusing on different remote sensing indices under GCC thresholds, the PWV fitted by each remote sensing index under 10% and 25% thresholds were significantly better than those before correction, especially 25%. Furthermore, it should be noted that the PWV fitted by the NDVI metrics was better compared to EVI and NIR<sub>v</sub> concerning near-surface phenology.

### 3.2. Wetland Vegetation Phenological Metrics Based on Landsat7/8 and Sentinel-2 Fusion

By comparing the vegetation index time series, It can be seen that there was obvious seasonal consistency between the satellite data and the near-surface observation (Figure 4). All four curves (GCC, EVI, NDVI, and NIR<sub>v</sub>) exhibited a similar bell-shaped pattern, wherein they initially increased slowly during spring, followed by a rapid increase, reaching their peak around July, and then gradually decreased until winter.

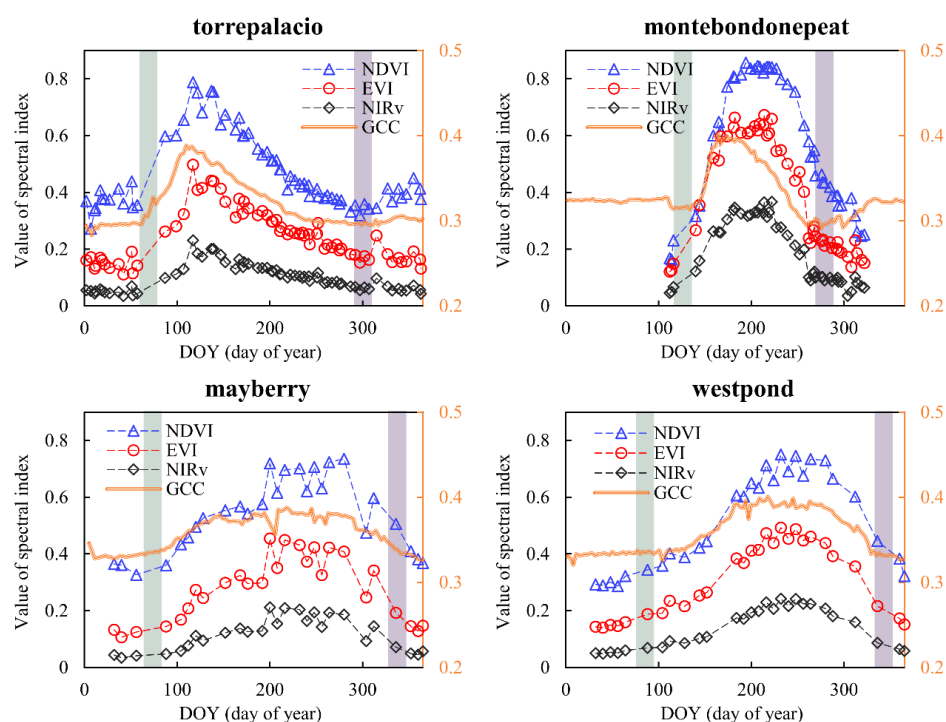


**Figure 4.** Time series of typical wetland sites based on LandSent30 and the PhenoCam network. The blue curve is NDVI, the red curve is EVI, the black curve is NIRv, the orange curve is GCC, the green and purple rectangles represent the SOS and EOS of the wetland vegetation, respectively, and all data are for 2018.

From the PWV results we generated (Figure 5), each site's fused LandSent30 data-based PWV was poorly matched with the near-surface PhenoCam-PWV overall, especially in LandSent30-EOS ( $R^2 < 0.4$  and  $RMSE > 30$  days). Here, we describe the LandSent30-based PWV in detail in three aspects: the satellite-estimated wetland phenology, different thresholds of GCC provided by the near-ground PhenoCam network, and the different remote sensing indices. In terms of phenological metrics, the SOS estimated based on remote sensing ( $R^2$  are both  $>0.4$ ) is usually better than the EOS ( $R^2$  are both  $<0.3$ ), and the overall RMSE of SOS at different thresholds was smaller than that of EOS. Different phenological metrics behaved differently in the interannual variation of PWV results during 2013–2018. Among them, the interannual variation of SOS was relatively small, with an overall distribution between 7 and 152 days and a concentration between 100 and 140 days. Nonetheless, EOS showed significant interannual variation, with an overall distribution ranging from 250 to 364 days and a concentration between 250 and 350 days.

From the different thresholds of the GCC, the estimated PWV under GCC-10th is significantly better than those of 25th and 50th, indicating that remote sensing can capture the earlier near-surface wetland vegetation changes. Regarding the performance of the three remote sensing indices, the NDVI is better than EVI and NIRv in SOS estimation and most of the results in EOS estimation, indicating that NDVI is more robust in monitoring and characterizing wetland vegetation phenology. From the different thresholds of remote sensing indices, the retrieved wetland vegetation phenological metrics from the fused data were poorly fitted at the threshold value of 10%. In comparison, the phenological estimated results at the thresholds of 25% and 50% were closer to the PhenoCam results, which also indicates that the early vegetation growth signals obtained based on remote sensing are susceptible to the presence of noise.

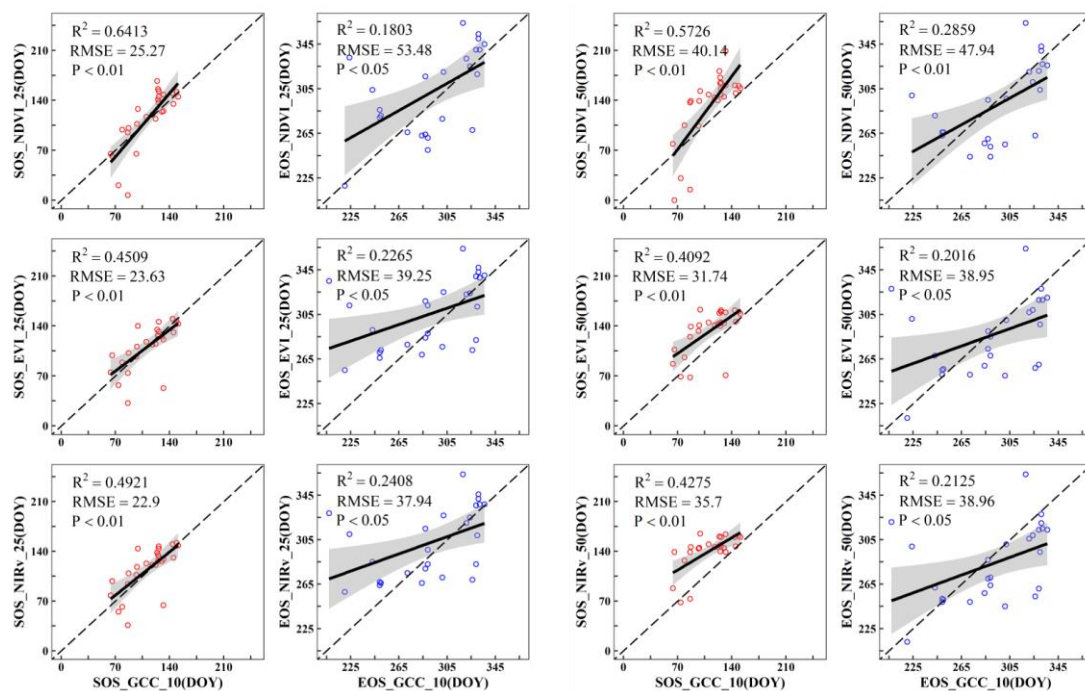


**Figure 5.** Comparison of wetland vegetation phenological periods from fused LandSent30 with near-surface phenological observations. The red hollow circles in the picture represent SOS, the blue hollow circles represent EOS.

### 3.3. Agreement between Different Remote Sensing Data and PhenoCam Phenology

We generated PWV results under each extracted buffer and analyzed the differences between remote sensing data sources (Tables S1–S7). It can be seen that there are large differences between satellite data at different resolutions and near-ground phenological observations in PWV. Overall, the accuracy of PWV generated by both LandSent30 and MODIS sensors of each wetland site is lower ( $R^2$  generally  $< 0.5$ ; RMSE is generally  $> 30$  days). However, with the increase in the extraction buffer of vegetation indices, the LandSent30-based PWV results within a 30–60 m buffer were significantly better than MODIS.

Within the LandSent 15 m buffer, the different remote sensing data sources-based PWV metrics (SOS, EOS) for the 11 wetland sites showed significant differences with the PhenoCam GCC-based SOS and EOS (GCC-SOS, GCC-EOS) (Table S1). Regarding the SOS, each vegetation index (NDVI, EVI, NIRv) phenological metrics retrieved using the LandSent30 data were better than that from the MODIS data source at different GCC thresholds. Different remotely sensed vegetation indices also showed slight differences in estimating wetland vegetation phenological metrics, among which NDVI was better fitted with  $R^2$  generally  $> 0.2$ . However, the performance of LandSent30 data sources was significantly poorer than MODIS on EOS. Moreover, the vegetation phenological metrics retrieved from different remote sensing data sources showed similar patterns within the 30 m, 45 m, and 60 m range of extracted buffer centered on the wetland site (Figure 6, Tables S2–S4). Regarding the SOS, each vegetation index phenological metric (NDVI, EVI, NIRv) estimated using LandSent30 data generally outperformed MODIS data sources at different GCC thresholds. However, there were slight differences in the performance of the remote sensing vegetation indices at their respective threshold ranges (10%, 25%, and 50%). Specifically, the SOS estimated based on each remote sensing vegetation index at the 50% amplitude threshold was better than those at 10% and 25%. Additionally, the SOS estimation of wetland vegetation was more consistent than the EOS estimation, which showed greater variance with the different data. Specifically, when compared with the GCC-EOS at a 10% threshold, we found that the consistency of the EOS by LandSent30-NDVI was significantly poorer than Landsat-EVI, NIRv and even worse than MODIS-EOS.

In contrast, in the comparison of GCC-EOS at 25% and 50% thresholds, the consistency of Landsat-NDVI was significantly better than MODIS-EOS, while the agreement of Landsat-EVI, NIRv was poor or not significant. The PWV-EOS results generated from LandSent30 data performed the same as those of 30 m, 45 m, and 60 m buffers in the extraction buffer of 90 m, 120 m, and 150 m centered on the wetland site (Tables S5–S7). However, the PWV-SOS fitted by each remote sensing index at different thresholds differed. Specifically, the fits of LandSent30-NDVI, NIRv compared to EVI were significantly worse than MODIS at the 10% and 25% thresholds of remote sensing vegetation index.

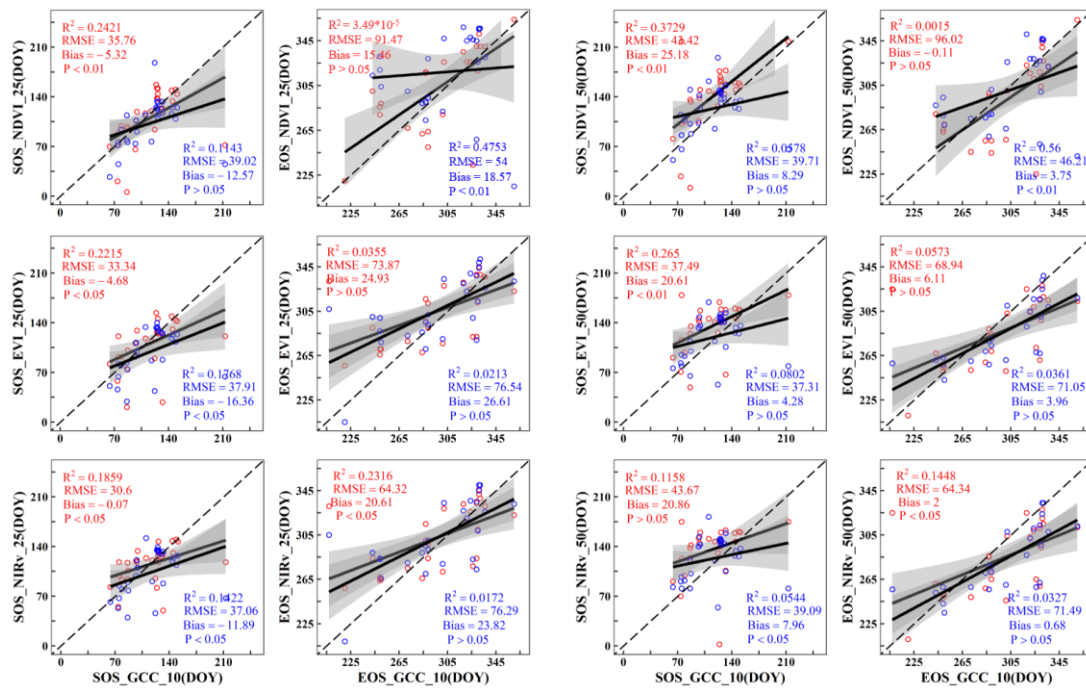


**Figure 6.** Comparison of wetland phenology based on LandSent30 and MODIS (30 m buffer). The red dots represent the consistency of LandSent30-based wetland phenology with near-ground GCC observations, and the blue dots represent MODIS. The x-axis represents the phenological metrics at the 10% threshold of the GCC index. The y-axis represents the phenological metrics at the 25% and 50% thresholds of NDVI, EVI, and NIRv, respectively.

In summary, with the increase in the extraction buffer of the wetland vegetation index (30–60 m), the fusion of high-resolution data from LandSent30 improved the accuracy of PWV retrieval.

### 3.4. Determination of Buffer and Threshold for LandSent30 Extract Phenology

In this study, we explored various greenness indices (EVI, NDVI, NIRv) using fused LandSent30 data to analyze all wetland sites located within the buffer zone. Vegetation indices were calculated for buffer ranges of 15 m, 30 m, 45 m, 60 m, 90 m, 120 m, and 150 m (refer to Figure S1 and Tables S1–S7). The study showed that the reliability of the satellite remote sensing-based vegetation phenology analysis decreased further as the buffer increased in the more heterogeneous wetland sites. The differences in PWV among buffers were not evident in the less heterogeneous wetland sites. In comparing remote sensing satellites with different resolutions, we found that the LandSent30-based PWV outperforms MODIS when the extraction buffer is 30–60 m.

Furthermore, we found that different threshold levels affect the consistency between different satellite remote sensing phenology and near-ground phenology (Table 5). In this study, we showed that the vast majority of LandSent30 fused phenology fits were significantly better than MODIS at the 50% threshold of the remote sensing indices. It

indicated that a 50% threshold for the remote sensing index threshold could filter out some of the noise in PWV retrieval and make it closer to the dynamic changes of near-surface wetland phenology.

**Table 5.** Comparison of wetland phenology results based on LandSent30 and MODIS (GCC-10% and RS-50% at 15 m buffer).

Remote Sensing Index	Statistic	SOS		EOS	
		LandSent30	MODIS	LandSent30	MODIS
NDVI	R <sup>2</sup>	0.35	0.04	0.14	0.41
	RMSE	46.92	39.85	57.80	37.07
	Bias	28.50	8.64	−9.68	−2.11
EVI	R <sup>2</sup>	0.24	0.06	0.12	0.30
	RMSE	35.12	37.35	46.02	39.09
	Bias	18.54	4.36	−4.11	−8.21
NIRv	R <sup>2</sup>	0.27	0.04	0.13	0.31
	RMSE	36.78	39.11	45.80	40.01
	Bias	24.46	8.00	−7.71	−11.68

## 4. Discussion

### 4.1. Performance of MODIS and LandSent30 in Wetland Phenology

Many studies have helped us track and analyze the annual changes in wetland vegetation [40,67,68]. For example, Jessica L. O’Connell et al. revealed the relationship between soil temperature and salt marsh phenology changes; they showed large inter-annual variability in phenology in the gcesapelo wetland, with green-up and dormant periods of 39–46 and 339–342 days, respectively, which is close to the 32–57 and 326–351 days in our study [69]. Jun Lu et al. retrieved the phenology of the montebondonepeat site through spectral and angular harmonization of Landsat-8, Sentinel-2, and Gaofen-1 data, and their seasonal variation was consistent with our results [70]. The above studies are very enlightening for our analysis of wetland vegetation phenology, but the scale of the study is relatively small. In this study, we selected Landsat-7/8, Sentinel-2, MODIS, and the near-ground PhenoCam network to further explore the performance of different resolution data sources in estimating global PWV. Recent studies have shown that the newly acquired sentinel-2A/B images combined with Landsat-7/8 images can further improve their temporal resolution to meet different challenges [71]. Therefore, we filtered the wetland site provided by the PhenoCam network and retrieved the PWV using the fused LandSent30 data. The estimated results also showed that the fused LandSent30 data improved the usability of remote sensing images and enhanced the quality of observations. Moreover, it has also been shown that the combination of the Landsat-8 Operational Land Imager (OLI) and the Sentinel-2 multispectral instrument (MSI) is also a good way to monitor the phenological changes of deciduous forests in North America [42,72].

By comparing MODIS and LandSent30 data-based wetland phenological metrics of different extracted buffers with those provided by the near-ground PhenoCam network, the results further confirmed that MODIS data performed more poorly than LandSent30 in retrieving PWV overall, especially in PWV-SOS. Although MODIS has a short revisit period and revisits almost daily, its coarse spatial resolution (250–500 m) leads to the observation of wetland features that usually contain mixed pixels elements [73], i.e., a combination of signals from various surrounding land covers [20]. This usually introduces noise into the time trajectory of vegetation indices extracted based on MODIS satellites, which is insufficient to monitor the fine-scale pattern of vegetation phenology changes in surface wetlands [72,74]. Additionally, this has also been confirmed in some satellite remote sensing phenology studies of agricultural land and deciduous forest sites [20], which means the resolution of the satellite limits the consistency between near-ground and satellite remote sensing data at the site.

Although LandSent30 data capture seasonal dynamics of surface vegetation at a finer scale compared to MODIS, this study revealed that the PWV of the fused LandSent30 data is also in poor agreement with the near-surface PhenoCam in complicated wetland landscapes, especially in PWV-EOS. This may be due to the more complex landscape composition of wetland vegetation and its vulnerability to climate extremes and anthropogenic management disturbances, which pose a challenge to the analysis of wetland phenology (Figure 7) [33,75]. In addition, the study has shown that the degree of agreement between remote sensing and surface observations varies by vegetation type [20]. Despite having the same vegetation type, landscape heterogeneity cannot be ignored when studying the retrieval of vegetation phenology. The presence of high landscape heterogeneity in the vicinity of wetland vegetation complicates the accurate identification and estimation of PWV. Future studies of global PWV need to weaken the effects of seasonal flooding and incorporate more advanced sensors (e.g., Sentinel-1, GF-3).



**Figure 7.** Seasonal variations of the surface landscape at the wetland site donanafuenteduque (from the PhenoCam network, 2019).

#### 4.2. Uncertainty in the PhenoCam Network

To our knowledge, the uncertainty of the PhenoCam site itself also exacerbates the difficulty of comparing the consistency between satellite remote sensing and near-ground observations. Specifically, the site locations provided by the PhenoCam network are based on the digital camera's location, not the camera's field of view (FOV). Our analysis of vegetation phenology is based on ROI images that are derived from the FOV. Therefore, areas with high landscape heterogeneity (as shown in Figure 8) are expected to have a larger estimation error for site-centered phenology. This means that the satellite-based observations of PWV are more comparable with GCC on homogeneous site landscapes. Therefore, this study first comprehensively evaluates the global wetland PhenoCam sites, mainly including camera location, the orientation of the camera FOV, and ROI settings. After removing the sites unsuitable for PWV retrieval, the satellite-based vegetation index extraction also fine-tunes the position of the more heterogeneous sites according to their camera ROI settings. With the above processing, we improved the consistency between satellite images and near-ground observations and further enhanced the wetland vegetation signal.



**Figure 8.** Ground images of the torrepalacio site and its ROI (from the PhenoCam network, 27 May 2018). The yellow boxes indicate the camera field of view ROI.

Furthermore, the image size of the satellite data is much larger than the FOV of the PhenoCam camera. We assumed that the near-ground vegetation phenology is consistent with the satellite remote sensing phenology, which only occurs when the landscape vegetation within the camera's FOV is representative of the corresponding satellite image [76]. This also highlights the need to calibrate the site location in advance, and S. T. Klosterman et al. showed that the EOS is usually later than near-ground phenology observations at sites with relatively little deciduous forest [52]. In addition, disturbances such as extreme weather events and human activities can easily shift the camera FOV, which may cause errors in the GCC time series in the variable ROI range.

#### 4.3. Implications and Future Work

This study mainly focused on global PWV metrics and compared satellite remote sensing (LandSent30, MODIS) at different resolutions with the RGB-based near-ground PhenoCam network. The accuracy of the PWV results is greatly affected by the high landscape heterogeneity of many wetland sites provided by the PhenoCam network. Therefore, in the future, we can reduce the interference of other land types and implement the PWV retrieval in fragmented areas with the help of remote sensing data with a higher spatial and temporal resolution, such as GF-12 and PlanetScope. Furthermore, this study found significant differences in PWV metrics (SOS, EOS) between the fused 30 m LandSent30 data and 500 m MODIS data. The mechanism underlying this difference should also be explored in the future. In future studies, we should also evaluate the ROI provided by PhenoCam in conjunction with higher-resolution satellite images to determine whether the ROI it sets is typical in the satellite-observed landscape. Specific solutions are proposed based on different situations, such as adjusting the site location or correcting the FOV of the camera. This work is also expected to improve our understanding of the observational consistency of near-ground and satellite remote sensing at different resolutions.

In addition, by overlaying the global 30 m wetland map with a fine classification system (GWL\_FCS30) data [77], we found that most wetland PhenoCam sites are of type marsh. The number of type mangrove and swamp wetland sites in the future can be increased appropriately. It will provide an essential platform for further understanding the dynamics of wetland vegetation changes and the differences of PWV under different habitats. On this basis, future studies can also further analyze the challenges faced in retrieving PWV in conjunction with flooding regimes and percent of open water.

## 5. Conclusions

Existing wetland vegetation phenology studies are limited compared to other forest and agroecosystems. Limited analyses of wetland phenology are mainly based on coarse-resolution remote sensing data, which cannot capture the complex character of the wetlands ecosystem. Here, we retrieved the PWV metrics at 11 wetland PhenoCam sites worldwide

based on LandSent30 fusion data and a double logistic function method. We then compared the phenology results from MODIS data using PhenoCam as a reference. The validation results show that our algorithm successfully retrieves the PWV in different climate zones. In general, the wetland phenology metrics generated by the LandSent30 fusion data perform better than MODIS sensors, and especially the correlation with near-ground is higher at sites with strong landscape heterogeneity. By comparing three remote sensing indices to the PhenoCam network, we found that the wetland SOS generated by the LandSent30 fusion data at a threshold of 50% for each remote sensing index is significantly better than that of MODIS. Our study is based on the multi-year dataset of the PhenoCam site network covering the global region, which establishes a bridge between the near-surface observations and the vegetation phenology estimation based on satellite remote sensing. It provides a reference for studying the PWV at a large scale.

**Supplementary Materials:** The following supporting information can be downloaded at: <https://www.mdpi.com/article/10.3390/rs15092413/s1>, Figure S1. Wetland vegetation phenology results based on the fusion of Landsat and Sentinel-2 (LandSent30) at 15m extracted buffer (10% of the green chromatic coordinate (GCC) amplitude). Figure S2. Wetland vegetation phenology results based on the fused LandSent30 at 15m buffer (25% of the GCC amplitude). Figure S3. Wetland vegetation phenology results based on the fused LandSent30 at 15m buffer (50% of the GCC amplitude). Table S1. Differences in the phenology of wetland vegetation (PWV) estimated by satellite remote sensing with different spatial resolutions at 15m buffer (10% of the GCC amplitude and 50% of the vegetation indices). Table S2. Differences in PWV estimated by satellite remote sensing with different spatial resolutions at 30m buffer (10% of the GCC amplitude and 25% of the vegetation indices). Table S3. Differences in PWV estimated by satellite remote sensing with different spatial resolutions at 45m buffer (10% of the GCC amplitude and 50% of the vegetation indices). Table S4. Differences in PWV estimated by satellite remote sensing with different spatial resolutions at 60m buffer (10% of the GCC amplitude and 50% of the vegetation indices). Table S5. Differences in PWV estimated by satellite remote sensing with different spatial resolutions at 90m buffer (25% of the GCC amplitude and 50% of the vegetation indices). Table S6. Differences in PWV estimated by satellite remote sensing with different spatial resolutions at 120m buffer (25% of the GCC amplitude and 50% of the vegetation indices). Table S7. Differences in PWV estimated by satellite remote sensing with different spatial resolutions at 150m buffer (25% of the GCC amplitude and 50% of the vegetation indices).

**Author Contributions:** Conceptualization, G.Z. (Geli Zhang), J.D. (Jinwei Dong); methodology and formal analysis, C.F. and J.Y.; writing—original draft preparation, review and editing, C.F., G.Z. (Geli Zhang), J.D. (Jinwei Dong), J.Y., G.Z. (Guosong Zhao), J.D. (Junhu Dai), M.Z., and R.L. All authors have read and agreed to the published version of the manuscript.

**Funding:** This research was funded by the National Key Research and Development Program of China (2018YFA0606100), the Strategic Priority Research Program (XDA26010202) of the Chinese Academy of Sciences (CAS), the National Natural Science Foundation of China (No. 42271375, 42201405, 42171115, 81961128002), and the CAS Youth Interdisciplinary Team Project (JCTD-2021-04).

**Data Availability Statement:** All the data in this study will be available on request from the corresponding author.

**Acknowledgments:** We thank the PhenoCAM network for providing the in situ observational data.

**Conflicts of Interest:** The authors declare no conflict of interest.

## References

1. Morissette, J.T.; Richardson, A.D.; Knapp, A.K.; Fisher, J.I.; Graham, E.A.; Abatzoglou, J.; Wilson, B.E.; Breshears, D.D.; Henebry, G.M.; Hanes, J.M.; et al. Tracking the rhythm of the seasons in the face of global change: Phenological research in the 21st century. *Front. Ecol. Environ.* **2009**, *7*, 253–260. [[CrossRef](#)]
2. Arnell, N.W.; Lloyd-Hughes, B. The global-scale impacts of climate change on water resources and flooding under new climate and socio-economic scenarios. *Clim. Change* **2014**, *122*, 127–140. [[CrossRef](#)]
3. Hu, S.J.; Niu, Z.G.; Chen, Y.F. Global Wetland Datasets: A Review. *Wetlands* **2017**, *37*, 807–817. [[CrossRef](#)]
4. Bureau, R.C. *Wetlands Values and Functions*; Ramsar Convention Bureau: Gland, Switzerland, 2001.

5. Dronova, I.; Gong, P.; Wang, L. Object-based analysis and change detection of major wetland cover types and their classification uncertainty during the low water period at Poyang Lake, China. *Remote Sens. Environ.* **2011**, *115*, 3220–3236. [[CrossRef](#)]
6. Shen, X.J.; Jiang, M.; Lu, X.G.; Liu, X.T.; Liu, B.; Zhang, J.Q.; Wang, X.W.; Tong, S.Z.; Lei, G.C.; Wang, S.Z.; et al. Aboveground biomass and its spatial distribution pattern of herbaceous marsh vegetation in China. *Sci. China-Earth Sci.* **2021**, *64*, 1115–1125. [[CrossRef](#)]
7. Halabisky, M.; Moskal, L.M.; Gillespie, A.; Hannam, M. Reconstructing semi-arid wetland surface water dynamics through spectral mixture analysis of a time series of Landsat satellite images (1984–2011). *Remote Sens. Environ.* **2016**, *177*, 171–183. [[CrossRef](#)]
8. Russi, D.; Brink, P.T.; Badura, T.; Farmer, A.; Badura, T.; Coates, D.; Förster, J.; Kumar, R.; Davidson, N. The Economics of Ecosystems and Biodiversity for Water and Wetlands. *IEEP Lond. Bruss.* **2013**, *78*, 118.
9. Bridgman, S.D.; Cadillo-Quiroz, H.; Keller, J.K.; Zhuang, Q.L. Methane emissions from wetlands: Biogeochemical, microbial, and modeling perspectives from local to global scales. *Glob. Change Biol.* **2013**, *19*, 1325–1346. [[CrossRef](#)] [[PubMed](#)]
10. Zhang, G.; Zhang, Y.; Dong, J.; Xiao, X. Green-up dates in the Tibetan Plateau have continuously advanced from 1982 to 2011. *Proc. Natl. Acad. Sci. USA* **2013**, *110*, 4309–4314. [[CrossRef](#)] [[PubMed](#)]
11. Kang, X.; Hao, Y.; Cui, X.; Chen, H.; Huang, S.; Du, Y.; Li, W.; Kardol, P.; Xiao, X.; Cui, L. Variability and Changes in Climate, Phenology, and Gross Primary Production of an Alpine Wetland Ecosystem. *Remote Sens.* **2016**, *8*, 391. [[CrossRef](#)]
12. Helfter, C.; Gondwe, M.; Murray-Hudson, M.; Makati, A.; Lunt, M.F.; Palmer, P.I.; Skiba, U. Phenology is the dominant control of methane emissions in a tropical non-forested wetland. *Nat. Commun.* **2022**, *13*, 133. [[CrossRef](#)] [[PubMed](#)]
13. Touzi, R.; IEEE. Wetland characterization using polarimetric RADARSAT-2 capability. In Proceedings of the IEEE International Geoscience and Remote Sensing Symposium (IGARSS), Denver, CO, USA, 31 July–4 August 2006; pp. 1639–1642.
14. Houlihan, J.E.; Keddy, P.A.; Makkay, K.; Findlay, C.S. The effects of adjacent land use on wetland species richness and community composition. *Wetlands* **2006**, *26*, 79–96. [[CrossRef](#)]
15. Gibbs, J.P. Wetland loss and biodiversity conservation. *Conserv. Biol.* **2000**, *14*, 314–317. [[CrossRef](#)]
16. Sparks, T.H.; Menzel, A. Observed changes in seasons: An overview. *Int. J. Climatol.* **2002**, *22*, 1715–1725. [[CrossRef](#)]
17. Hufkens, K.; Melaas, E.K.; Mann, M.L.; Foster, T.; Ceballos, F.; Robles, M.; Kramer, B. Monitoring crop phenology using a smartphone based near-surface remote sensing approach. *Agric. For. Meteorol.* **2019**, *265*, 327–337. [[CrossRef](#)]
18. Seyednasrollah, B.; Young, A.M.; Hufkens, K.; Milliman, T.; Friedl, M.A.; Frohling, S.; Richardson, A.D. Tracking vegetation phenology across diverse biomes using Version 2.0 of the PhenoCam Dataset. *Sci. Data* **2019**, *6*, 222. [[CrossRef](#)]
19. Zeng, L.L.; Wardlow, B.D.; Xiang, D.X.; Hu, S.; Li, D.R. A review of vegetation phenological metrics extraction using time-series, multispectral satellite data. *Remote Sens. Environ.* **2020**, *237*, 111511. [[CrossRef](#)]
20. Richardson, A.D.; Hufkens, K.; Milliman, T.; Frohling, S. Intercomparison of phenological transition dates derived from the PhenoCam Dataset V1.0 and MODIS satellite remote sensing. *Sci. Rep.* **2018**, *8*, 5679. [[CrossRef](#)]
21. Richardson, A.D.; Klosterman, S.; Toomey, M. Near-Surface Sensor-Derived Phenology. In *Phenology: An Integrative Environmental Science*; Springer Netherlands: Dordrecht, The Netherlands, 2013.
22. Garrity, S.R.; Bohrer, G.; Maurer, K.D.; Mueller, K.L.; Vogel, C.S.; Curtis, P.S. A comparison of multiple phenology data sources for estimating seasonal transitions in deciduous forest carbon exchange. *Agric. For. Meteorol.* **2011**, *151*, 1741–1752. [[CrossRef](#)]
23. Huemmrich, K.F.; Black, T.A.; Jarvis, P.G.; McCaughey, J.H.; Hall, F.G. High temporal resolution NDVI phenology from micrometeorological radiation sensors. *J. Geophys. Res. Atmos.* **1999**, *104*, 27935–27944. [[CrossRef](#)]
24. Soudani, K.; Hmimina, G.; Delpierre, N.; Pontailier, J.Y.; Aubinet, M.; Bonal, D.; Caquet, B.; de Grandcourt, A.; Burban, B.; Flechard, C.; et al. Ground-based Network of NDVI measurements for tracking temporal dynamics of canopy structure and vegetation phenology in different biomes. *Remote Sens. Environ.* **2012**, *123*, 234–245. [[CrossRef](#)]
25. Ahl, D.E.; Gower, S.T.; Burrows, S.N.; Shabanov, N.V.; Myneni, R.B.; Knyazikhin, Y. Monitoring spring canopy phenology of a deciduous broadleaf forest using MODIS. *Remote Sens. Environ.* **2006**, *104*, 88–95. [[CrossRef](#)]
26. Zhang, Q.; Xiao, X.; Braswell, B.; Linder, E.; Ollinger, S.; Smith, M.-L.; Jenkins, J.P.; Baret, F.; Richardson, A.D.; Moore, B.; et al. Characterization of seasonal variation of forest canopy in a temperate deciduous broadleaf forest, using daily MODIS data. *Remote Sens. Environ.* **2006**, *105*, 189–203. [[CrossRef](#)]
27. Xin, Q.C.; Broich, M.; Zhu, P.; Gong, P. Modeling grassland spring onset across the Western United States using climate variables and MODIS-derived phenology metrics. *Remote Sens. Environ.* **2015**, *161*, 63–77. [[CrossRef](#)]
28. Cui, T.F.; Martz, L.; Zhao, L.; Guo, X.L. Investigating the impact of the temporal resolution of MODIS data on measured phenology in the prairie grasslands. *Giscience Remote Sens.* **2020**, *57*, 395–410. [[CrossRef](#)]
29. Zhang, G.; Xiao, X.; Biradar, C.M.; Dong, J.; Qin, Y.; Menarguez, M.A.; Zhou, Y.; Zhang, Y.; Jin, C.; Wang, J.; et al. Spatiotemporal patterns of paddy rice croplands in China and India from 2000 to 2015. *Sci. Total. Environ.* **2017**, *579*, 82–92. [[CrossRef](#)] [[PubMed](#)]
30. Pastor-Guzman, J.; Dash, J.; Atkinson, P.M. Remote sensing of mangrove forest phenology and its environmental drivers. *Remote Sens. Environ.* **2018**, *205*, 71–84. [[CrossRef](#)]
31. Hmimina, G.; Dufrene, E.; Pontailier, J.Y.; Delpierre, N.; Aubinet, M.; Caquet, B.; de Grandcourt, A.; Burban, B.; Flechard, C.; Granier, A.; et al. Evaluation of the potential of MODIS satellite data to predict vegetation phenology in different biomes: An investigation using ground-based NDVI measurements. *Remote Sens. Environ.* **2013**, *132*, 145–158. [[CrossRef](#)]
32. Khare, S.; Deslauriers, A.; Morin, H.; Latifi, H.; Rossi, S. Comparing Time-Lapse PhenoCams with Satellite Observations across the Boreal Forest of Quebec, Canada. *Remote Sens.* **2022**, *14*, 100. [[CrossRef](#)]

33. Kearney, M.S.; Stutzer, D.; Turpie, K.; Stevenson, J.C. The Effects of Tidal Inundation on the Reflectance Characteristics of Coastal Marsh Vegetation. *J. Coast. Res.* **2009**, *25*, 1177–1186. [[CrossRef](#)]
34. Byrd, K.B.; O’Connell, J.L.; Di Tommaso, S.; Kelly, M. Evaluation of sensor types and environmental controls on mapping biomass of coastal marsh emergent vegetation. *Remote Sens. Environ.* **2014**, *149*, 166–180. [[CrossRef](#)]
35. Miller, G.J.; Dronova, I.; Oikawa, P.Y.; Knox, S.H.; Windham-Myers, L.; Shahan, J.; Stuart-Haentjens, E. The Potential of Satellite Remote Sensing Time Series to Uncover Wetland Phenology under Unique Challenges of Tidal Setting. *Remote Sens.* **2021**, *13*, 28. [[CrossRef](#)]
36. Melaas, E.K.; Friedl, M.A.; Zhu, Z. Detecting interannual variation in deciduous broadleaf forest phenology using Landsat TM/ETM plus data. *Remote Sens. Environ.* **2013**, *132*, 176–185. [[CrossRef](#)]
37. Bolton, D.K.; Gray, J.M.; Melaas, E.K.; Moon, M.; Eklundh, L.; Friedl, M.A. Continental-scale land surface phenology from harmonized Landsat 8 and Sentinel-2 imagery. *Remote Sens. Environ.* **2020**, *240*, 111685. [[CrossRef](#)]
38. Liu, Y.; Hill, M.J.; Zhang, X.Y.; Wang, Z.S.; Richardson, A.D.; Hufkens, K.; Filippa, G.; Baldocchi, D.D.; Ma, S.Y.; Verfaillie, J.; et al. Using data from Landsat, MODIS, VIIRS and PhenoCams to monitor the phenology of California oak/grass savanna and open grassland across spatial scales. *Agric. For. Meteorol.* **2017**, *237*, 311–325. [[CrossRef](#)]
39. Dong, J.W.; Xiao, X.M.; Kou, W.L.; Qin, Y.W.; Zhang, G.L.; Li, L.; Jin, C.; Zhou, Y.T.; Wang, J.; Biradar, C.; et al. Tracking the dynamics of paddy rice planting area in 1986–2010 through time series Landsat images and phenology-based algorithms. *Remote Sens. Environ.* **2015**, *160*, 99–113. [[CrossRef](#)]
40. Wang, X.; Xiao, X.; Zou, Z.; Hou, L.; Qin, Y.; Dong, J.; Doughty, R.B.; Chen, B.; Zhang, X.; Chen, Y.; et al. Mapping coastal wetlands of China using time series Landsat images in 2018 and Google Earth Engine. *ISPRS J. Photogramm. Remote Sens.* **2020**, *163*, 312–326. [[CrossRef](#)] [[PubMed](#)]
41. Pan, L.; Xia, H.M.; Yang, J.; Niu, W.H.; Wang, R.M.; Song, H.Q.; Guo, Y.; Qin, Y.C. Mapping cropping intensity in Huaihe basin using phenology algorithm, all Sentinel-2 and Landsat images in Google Earth Engine. *Int. J. Appl. Earth Obs. Geoinf.* **2021**, *102*, 13. [[CrossRef](#)]
42. Liu, L.; Xiao, X.; Qin, Y.; Wang, J.; Xu, X.; Hu, Y.; Qiao, Z. Mapping cropping intensity in China using time series Landsat and Sentinel-2 images and Google Earth Engine. *Remote Sens. Environ.* **2020**, *239*, 111624. [[CrossRef](#)]
43. Zhang, J.; Zhao, J.J.; Wang, Y.Q.; Zhang, H.Y.; Zhang, Z.X.; Guo, X.Y. Comparison of land surface phenology in the Northern Hemisphere based on AVHRR GIMMS3g and MODIS datasets. *ISPRS J. Photogramm. Remote Sens.* **2020**, *169*, 1–16. [[CrossRef](#)]
44. Li, X.; Zhou, Y.; Meng, L.; Asrar, G.R.; Lu, C.; Wu, Q. A dataset of 30 m annual vegetation phenology indicators (1985–2015) in urban areas of the conterminous United States. *Earth Syst. Sci. Data* **2019**, *11*, 881–894. [[CrossRef](#)]
45. Andresen, C.G.; Tweedie, C.E.; Loughheed, V.L. Climate and nutrient effects on Arctic wetland plant phenology observed from phenocams. *Remote Sens. Environ.* **2018**, *205*, 46–55. [[CrossRef](#)]
46. Baumann, M.; Ozdogan, M.; Richardson, A.D.; Radeloff, V.C. Phenology from Landsat when data is scarce: Using MODIS and Dynamic Time-Warping to combine multi-year Landsat imagery to derive annual phenology curves. *Int. J. Appl. Earth Obs. Geoinf.* **2017**, *54*, 72–83. [[CrossRef](#)]
47. Moon, M.; Zhang, X.Y.; Henebry, G.M.; Liu, L.L.; Gray, J.M.; Melaas, E.K.; Friedl, M.A. Long-term continuity in land surface phenology measurements: A comparative assessment of the MODIS land cover dynamics and VIIRS land surface phenology products. *Remote Sens. Environ.* **2019**, *226*, 74–92. [[CrossRef](#)]
48. Ling, Y.X.; Teng, S.W.; Liu, C.; Dash, J.; Morris, H.; Pastor-Guzman, J. Assessing the Accuracy of Forest Phenological Extraction from Sentinel-1 C-Band Backscatter Measurements in Deciduous and Coniferous Forests. *Remote Sens.* **2022**, *14*, 14. [[CrossRef](#)]
49. Liu, C.; Zhang, Q.; Tao, S.Q.; Qi, J.G.; Ding, M.J.; Guan, Q.H.; Wu, B.F.; Zhang, M.; Nabil, M.; Tian, F.Y.; et al. A new framework to map fine resolution cropping intensity across the globe: Algorithm, validation, and implication. *Remote Sens. Environ.* **2020**, *251*, 17. [[CrossRef](#)]
50. Richardson, A.D.; Hufkens, K.; Milliman, T.; Aubrecht, D.M.; Chen, M.; Gray, J.M.; Johnston, M.R.; Keenan, T.F.; Klosterman, S.T.; Kosmala, M.; et al. Tracking vegetation phenology across diverse North American biomes using PhenoCam imagery. *Sci. Data* **2018**, *5*, 180028. [[CrossRef](#)] [[PubMed](#)]
51. Keenan, T.F.; Richardson, A.D. The timing of autumn senescence is affected by the timing of spring phenology: Implications for predictive models. *Glob. Change Biol.* **2015**, *21*, 2634–2641. [[CrossRef](#)]
52. Klosterman, S.T.; Hufkens, K.; Gray, J.M.; Melaas, E.; Sonnentag, O.; Lavine, I.; Mitchell, L.; Norman, R.; Friedl, M.A.; Richardson, A.D. Evaluating remote sensing of deciduous forest phenology at multiple spatial scales using PhenoCam imagery. *Biogeosciences* **2014**, *11*, 4305–4320. [[CrossRef](#)]
53. Seyednasrollah, B.; Young, A.M.; Hufkens, K.; Milliman, T.; Friedl, M.A.; Frohling, S.; Richardson, A.D.; Abraha, M.; Allen, D.W.; Apple, M.; et al. *PhenoCam Dataset v2.0: Vegetation Phenology from Digital Camera Imagery, 2000–2018*; ORNL DAAC: Oak Ridge, TN, USA, 2019. [[CrossRef](#)]
54. Richardson, A.D.; Braswell, B.H.; Hollinger, D.Y.; Jenkins, J.P.; Ollinger, S.V. Near-surface remote sensing of spatial and temporal variation in canopy phenology. *Ecol. Appl.* **2009**, *19*, 1417–1428. [[CrossRef](#)] [[PubMed](#)]
55. Sonnentag, O.; Hufkens, K.; Teshera-Sterne, C.; Young, A.M.; Friedl, M.; Braswell, B.H.; Milliman, T.; O’Keefe, J.; Richardson, A.D. Digital repeat photography for phenological research in forest ecosystems. *Agric. For. Meteorol.* **2012**, *152*, 159–177. [[CrossRef](#)]

56. Young, A.M.; Friedl, M.A.; Seyednasrollah, B.; Beamesderfer, E.; Carrillo, C.M.; Li, X.L.; Moon, M.; Arain, M.A.; Baldocchi, D.D.; Blanken, P.D.; et al. Seasonality in aerodynamic resistance across a range of North American ecosystems. *Agric. For. Meteorol.* **2021**, *310*, 108613. [[CrossRef](#)]
57. Roy, D.P.; Wulder, M.A.; Loveland, T.R.; Woodcock, C.E.; Allen, R.G.; Anderson, M.C.; Helder, D.; Irons, J.R.; Johnson, D.M.; Kennedy, R.; et al. Landsat-8: Science and product vision for terrestrial global change research. *Remote Sens. Environ.* **2014**, *145*, 154–172. [[CrossRef](#)]
58. Mas, J.F.; de Araujo, R.S. Assessing Landsat Images Availability and Its Effects on Phenological Metrics. *Forests* **2021**, *12*, 574. [[CrossRef](#)]
59. Irons, J.R.; Dwyer, J.L.; Barsi, J.A. The next Landsat satellite: The Landsat Data Continuity Mission. *Remote Sens. Environ.* **2012**, *122*, 11–21. [[CrossRef](#)]
60. Drusch, M.; Del Bello, U.; Carlier, S.; Colin, O.; Fernandez, V.; Gascon, F.; Hoersch, B.; Isola, C.; Laberinti, P.; Martimort, P.; et al. Sentinel-2: ESA's Optical High-Resolution Mission for GMES Operational Services. *Remote Sens. Environ.* **2012**, *120*, 25–36. [[CrossRef](#)]
61. Frantz, D. FORCE—Landsat + Sentinel-2 Analysis Ready Data and Beyond. *Remote Sens.* **2019**, *11*, 1124. [[CrossRef](#)]
62. Schaaf, C.B.; Liu, J.C.; Gao, F.; Strahler, A.H. *Aqua and Terra MODIS Albedo and Reflectance Anisotropy Products*; Springer: Dordrecht, The Netherlands, 2011; Volume 11, pp. 549–561.
63. Zhang, X.Y.; Liu, L.L.; Liu, Y.; Jayavelu, S.; Wang, J.M.; Moon, M.; Henebry, G.M.; Friedl, M.A.; Schaaf, C.B. Generation and evaluation of the VIIRS land surface phenology product. *Remote Sens. Environ.* **2018**, *216*, 212–229. [[CrossRef](#)]
64. Zhang, H.K.; Roy, D.P.; Yan, L.; Li, Z.; Huang, H.; Vermote, E.; Skakun, S.; Roger, J.-C. Characterization of Sentinel-2A and Landsat-8 top of atmosphere, surface, and nadir BRDF adjusted reflectance and NDVI differences. *Remote Sens. Environ.* **2018**, *215*, 482–494. [[CrossRef](#)]
65. Yang, J.; Dong, J.; Xiao, X.; Dai, J.; Wu, C.; Xia, J.; Zhao, G.; Zhao, M.; Li, Z.; Zhang, Y.; et al. Divergent shifts in peak photosynthesis timing of temperate and alpine grasslands in China. *Remote Sens. Environ.* **2019**, *233*, 111395. [[CrossRef](#)]
66. Chen, J.; Jonsson, P.; Tamura, M.; Gu, Z.H.; Matsushita, B.; Eklundh, L. A simple method for reconstructing a high-quality NDVI time-series data set based on the Savitzky-Golay filter. *Remote Sens. Environ.* **2004**, *91*, 332–344. [[CrossRef](#)]
67. Dong, J.; Xiao, X.; Menarguez, M.A.; Zhang, G.; Qin, Y.; Thau, D.; Biradar, C.; Moore, B., III. Mapping paddy rice planting area in northeastern Asia with Landsat 8 images, phenology-based algorithm and Google Earth Engine. *Remote Sens. Environ.* **2016**, *185*, 142–154. [[CrossRef](#)] [[PubMed](#)]
68. Li, H.X.; Wang, C.Z.; Yu, Q.Y.; Smith, E. Spatiotemporal assessment of potential drivers of salt marsh dieback in the North Inlet-Winyah Bay estuary, South Carolina (1990–2019). *J. Environ. Manag.* **2022**, *313*, 114907. [[CrossRef](#)] [[PubMed](#)]
69. O'Connell, J.L.; Alber, M.; Pennings, S.C. Microspatial Differences in Soil Temperature Cause Phenology Change on Par with Long-Term Climate Warming in Salt Marshes. *Ecosystems* **2020**, *23*, 498–510. [[CrossRef](#)]
70. Lu, J.; He, T.; Song, D.X.; Wang, C.Q. Land Surface Phenology Retrieval through Spectral and Angular Harmonization of Landsat-8, Sentinel-2 and Gaofen-1 Data. *Remote Sens.* **2022**, *14*, 1296. [[CrossRef](#)]
71. Zhang, X.; Xiao, X.; Qiu, S.; Xu, X.; Wang, X.; Chang, Q.; Wu, J.; Li, B. Quantifying latitudinal variation in land surface phenology of *Spartina alterniflora* saltmarshes across coastal wetlands in China by Landsat 7/8 and Sentinel-2 images. *Remote Sens. Environ.* **2022**, *269*, 112810. [[CrossRef](#)]
72. Melaas, E.K.; Sulla-Menashe, D.; Gray, J.M.; Black, T.A.; Morin, T.H.; Richardson, A.D.; Friedl, M.A. Multisite analysis of land surface phenology in North American temperate and boreal deciduous forests from Landsat. *Remote Sens. Environ.* **2016**, *186*, 452–464. [[CrossRef](#)]
73. De Jong, R.; Verbesselt, J.; Zeileis, A.; Schaepman, M.E. Shifts in Global Vegetation Activity Trends. *Remote Sens.* **2013**, *5*, 1117–1133. [[CrossRef](#)]
74. Wulder, M.A.; White, J.C.; Loveland, T.R.; Woodcock, C.E.; Belward, A.S.; Cohen, W.B.; Fosnight, E.A.; Shaw, J.; Masek, J.G.; Roy, D.P. The global Landsat archive: Status, consolidation, and direction. *Remote Sens. Environ.* **2016**, *185*, 271–283. [[CrossRef](#)]
75. O'Connell, J.L.; Alber, M. A smart classifier for extracting environmental data from digital image time-series: Applications for PhenoCam data in a tidal salt marsh. *Environ. Model. Softw.* **2016**, *84*, 134–139. [[CrossRef](#)]
76. Cescatti, A.; Marcolla, B.; Vannan, S.K.S.; Pan, J.Y.; Roman, M.O.; Yang, X.Y.; Ciaia, P.; Cook, R.B.; Law, B.E.; Matteucci, G.; et al. Intercomparison of MODIS albedo retrievals and in situ measurements across the global FLUXNET network. *Remote Sens. Environ.* **2012**, *121*, 323–334. [[CrossRef](#)]
77. Zhang, X.; Liu, L.Y.; Zhao, T.T.; Chen, X.D.; Lin, S.R.; Wang, J.Q.; Mi, J.; Liu, W.D. GWL\_FCS30: A global 30 m wetland map with a fine classification system using multi-sourced and time-series remote sensing imagery in 2020. *Earth Syst. Sci. Data.* **2023**, *15*, 265–293. [[CrossRef](#)]

**Disclaimer/Publisher's Note:** The statements, opinions and data contained in all publications are solely those of the individual author(s) and contributor(s) and not of MDPI and/or the editor(s). MDPI and/or the editor(s) disclaim responsibility for any injury to people or property resulting from any ideas, methods, instructions or products referred to in the content.